

Bifunctional Zn Coordination Polymers for High-Performance Fluorescence Turn-On Detection of L-Glutamate and Adsorption of Malachite Green in Aqueous Medium

Published as part of a *Crystal Growth & Design* virtual special issue Celebrating John N. Sherwood, Pioneer in Organic and Molecular Crystals.

Sai Ma, Lingling Gao,* Yujuan Zhang, and Tuoping Hu*



Cite This: *Cryst. Growth Des.* 2023, 23, 2455–2462



Read Online

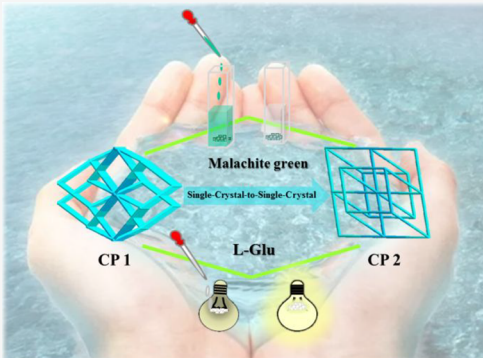
ACCESS |

Metrics & More

Article Recommendations

Supporting Information

ABSTRACT: Two time-induced Zn(II) coordination polymers (CPs), namely $\{[\text{Zn}(\text{BIPA-TC})_{0.5}(1,3\text{-bimb})]\cdot0.75\text{DMF}\}_n$ (**1**) and $\{[\text{Zn}(\text{BIPA-TC})_{0.5}(1,3\text{-bimb})]\cdot0.5\text{EtOH}\cdot\text{DMF}\cdot\text{H}_2\text{O}\}_n$ (**2**) were constructed based on 5,5'-(1,3,6,8-tetraoxybenzo[3,8]phenanthroline 2–7-substituent) bis-1,3-benzoic acid (H₄BIPA-TC) and zinc salts. The structure analysis showed that **1** is 3D networks with the point symbol $\{6^2, 8^4\} \{6^4, 8^2\}_2$ and **2** is 2D layered structures with the point symbol of $\{4, 6^4, 8\}_2 \{4^2, 6^4\}$. Interestingly, the transformation from single crystal **1** to **2** is only due to the prolongation of reaction time, which can be confirmed by structural analysis and powder X-ray diffraction patterns. Meanwhile, the fluorescence sensing properties of **1** and **2** showed that both **1** and **2** had high sensitivity for L-glutamate with limits of detection of 0.10 (**1**) and 0.13 μM (**2**). The fluorescence mechanism analysis showed that the fluorescence enhancement of **1** and **2** is attributed to absorbance caused enhancement and photoinduced electron transfer. In addition, **1** and **2** can also be used as recyclable adsorbents to remove malachite green (MG) in aqueous medium. The adsorption isotherms and kinetics of both **1** and **2** follow the Freundlich model and the quasi-second-order kinetic model, respectively. The maximum equilibrium adsorption capacities of **1** and **2** for MG can reach 351.06 and 250.45 mg/g, respectively. The excellent adsorption properties of **1**/**2** for MG can be attributed to $\pi-\pi$ interaction, hydrogen bonding, and electrostatic interaction between **1**/**2** and the MG molecule. Therefore, **1** and **2** have potential application prospects in fluorescence recognition and adsorption.



1. INTRODUCTION

Coordination polymers (CPs) have attracted much attention in recent years for their potential application prospects in gas storage and separation,^{1,2} magnetism,³ fluorescence recognition, and drug release.^{4,5} It is well-known that the performance of CPs depends greatly on their structural features, such as large conjugated structure, porosity, and diverse topology.^{6,7} Therefore, from the perspective of crystal engineering, the construction of CPs with unique frameworks and excellent properties is one of the research hotspots.^{8,9} In the self-assembly process of a CP, the reasonable choice of metal centers and organic ligands largely determines the topology and performance. On the one hand, the transition metal ions (Cd^{2+} and Zn^{2+}) with d^{10} configuration can improve the radiation emission of a CP by metal to ligand charge transfer.¹⁰ On the other hand, aromatic poly(carboxylic acid) ligands can construct CPs with high dimensions due to their possibly adopting versatile coordination modes.^{11,12} In addition, the final structure of a CP is also affected by external factors, such as reaction temperature, pH value, solvent system, and reaction time.^{13,14}

Subtle changes in any one of these factors can lead to changes in the structural dimensions and properties of CPs. For example, two solvent-induced Zn-MOFs with various structures and stabilities were synthesized, and Zn-MOF with *apo* topology can be used for detection of nitrobenzene in the environment.¹⁵ Meanwhile, three temperature-induced Co-CPs with three different configurations were constructed, which exhibited different magnetic properties between the Co chains.¹⁶ In particular, reaction time has a great influence on the structures of CPs, which can regulate the transformation between kinetic products and thermodynamic products, thus changing the properties of CPs. Therefore, it is worthwhile to systematically

Received: November 30, 2022

Revised: February 10, 2023

Published: March 1, 2023



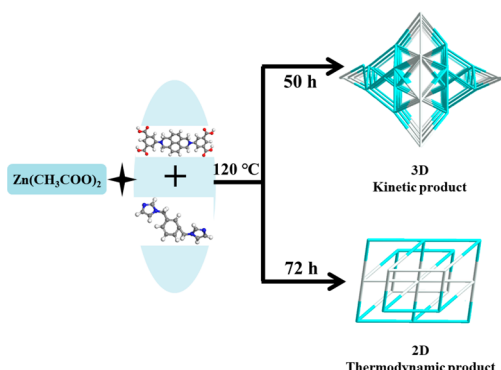
study the effects of external conditions on the structures and properties of CPs under the condition of fixing the metal center and ligand.

In medicine, the amount of L-glutamate (L-Glu) in the human body is closely related to various neurological disorders, Parkinson's disease, and amyotrophic lateral sclerosis.¹⁷ Because of the complex operation, time requirements, and high cost of traditional methods for the detection of glutamate, researchers are encouraged to seek a simple, rapid, and economic detection method.¹⁸ Recently, due to the convenience and economy of fluorescence recognition, researchers generally believe that CPs have the potential prospect for fluorescence recognition. For example, the Zhao group reported a sensor based on fluorescence quenching for the detection of L-Glu in aqueous solution.¹⁹ Compared with fluorescence turn-off sensors, fluorescence turn-on sensors have the advantages of easy recognition in a dark background and elimination of false responses of sensor signals, which have attracted many researchers' attention.²⁰

Malachite green (MG) is one of the most commonly used dyes in the textile and aquaculture industries.^{21,22} However, exposure to excessive amounts of MG can damage human health, leading to mutations, abnormalities, and cancer. Therefore, it is necessary to remove excess MG from the environment to improve people's standard of living. So far, many methods, such as coagulation and flocculation, biotherapy, precipitation, photocatalytic degradation, ozonation, and adsorption, have been applied to remove MG from aqueous media.^{23,24} Adsorption is considered to be a simple and effective method.^{25,26} Generally, the adsorbents reported mainly include molecular sieves, exchange resins, activated carbon, and CPs.²⁷ Among them, CPs have attracted extensive attention from researchers because of their controllable pore sizes and large specific surface areas.

On the basis of the above situation, two time-induced Zn(II)-CPs, namely, $\{[Zn(BIPA-TC)_{0.5}(1,3-bimb)] \cdot 0.75DMF\}_n$ (**1**) and $\{[Zn(BIPA-TC)_{0.5}(1,3-bimb)] \cdot 0.5EtOH \cdot DMF \cdot H_2O\}_n$ (**2**), have been constructed based on 5,5'-(1,3,6,8-tetraoxybenzo-[3,8]phenanthroline 2-7-substituent) bis-1,3-benzoic acid (H₄BIPA-TC), 1,3-bis(imidazol-1-ylmethyl)benzene (1,3-bimb), and zinc salts (Scheme 1). Then, Zn(II)-CPs **1** and **2** were characterized by single crystal X-ray diffraction, powder X-ray diffraction (PXRD), thermogravimetry (TG), and elemental analysis (EA). Meanwhile, the fluorescence properties of Zn(II)-CPs were explored. Furthermore, the fluorescence enhancement mechanisms were further revealed by a series of experiments and density functional theory (DFT) calculations. In addition, the

Scheme 1. Syntheses of CPs **1 and **2****



adsorption behaviors of Zn-CPs for cationic dyes have been studied. Finally, the adsorption performance of Zn-CPs for MG was investigated from the perspectives of adsorption isotherm and kinetics.

2. EXPERIMENTAL SECTION

2.1. Materials and Methods. H₄BIPA-TC and 1,3-bimb ligands were purchased by Jinan Henghua Chemical Co., Ltd.. All solvents and chemical materials were commercially obtained without further purification. Powder X-ray diffraction (PXRD) of samples was measured using a D/MAX-2500 X-ray diffractometer. Thermogravimetric analyses (TGA) were collected on a NETZSCH STA 2500 instrument under a N_2 atmosphere. Luminescence spectra were recorded at $25\text{ }^\circ\text{C}$ on an EDINBURGH FSS fluorescence spectrophotometer. The N_2 adsorption and desorption isotherms of **1** and **2** were recorded by an ASAP 2020 Plus analyzer, and the absorbances of **1** and **2** for dye molecules were tested by a Shimadzu UV-vis spectrophotometer (UV-2600). Scanning electron microscopy (SEM) and energy dispersive spectrometer (EDS) images were measured by a Zeiss Supra 55. Other instruments and test conditions are the same as those of reported studies.²⁸

2.2. Synthesis of $\{[Zn(BIPA-TC)_{0.5}(1,3-bimb)] \cdot 0.75DMF\}_n$ (1**) and $\{[Zn(BIPA-TC)_{0.5}(1,3-bimb)] \cdot 0.5EtOH \cdot DMF \cdot H_2O\}_n$ (**2**).** The mixture of $Zn(NO_3)_2 \cdot 6H_2O$ (0.004 mmol, 1.7 mg), H₄BIPA-TC (0.001 mmol, 0.6 mg), and 1,3-bimb (0.002 mmol, 0.5 mg) was added to a Teflon-lined reaction tank with a mixed solution of 1 mL of EtOH/DMF/H₂O (v/v/v = 1/1/2), which was heated to $120\text{ }^\circ\text{C}$ for 50 h to prepare lemon-yellow petal crystals of **1** (yield 42.1% based on H₄BIPA-TC). Elemental analysis (%) calcd for $C_{29}H_{19}N_5O_6Zn$: C, 58.15; H, 3.19; O, 16.03; N, 11.69; Zn, 10.92. Found: C, 58.18; H, 3.22; O, 16.20; N, 11.80; Zn, 10.95.

The synthesis method of **2** was basically similar to that of **1** except for the solvothermal reaction time of 72 h. Lemon-yellow block crystals of **2** were gained (yield 37.5%). Elemental analysis (%) calcd for $C_{29}H_{19}N_5O_6Zn$: C, 58.15; H, 3.19; O, 16.03; N, 11.69; Zn, 10.92. Found: C, 58.19; H, 3.20; O, 16.19; N, 11.78; Zn, 10.79.

2.3. Fluorescent Tests. Samples in the amount of 2 mg were added to 2 mL of different amino acid aqueous solutions (1 mM, L-proline; L-Glu; L-arginine; L-phenylalanine; L-aspartate; L-lysine; L-valine; L-cysteine; L-histidine; L-tyrosine; and L-leucine) to form a uniform suspension after ultrasonic dispersion for 10 min. For all measurements, the emission spectra of ligands and compounds were measured from 400 to 750 nm with an excitation wavelength of 420 nm.

2.4. The Activating Treatment of Sample. CPs **1** and **2** in the amount of 120 mg were successively dispersed in CH_3OH and CH_2Cl_2 for 3 days, and the solvent was changed every 8 h to exchange free solvent molecules in their channels. Then **1** and **2** were heated under vacuum at $100\text{ }^\circ\text{C}$ for 10 h to obtain activated samples for testing.

2.5. Dye Adsorption. Different cationic dyes including malachite green (MG, 0.01 mmol, 3.60 mg), methyl orange (MO, 0.01 mmol, 3.30 mg), methylene blue (MB, 0.01 mmol, 3.70 mg), and Rhodamine B (RhB, 0.01 mmol, 4.80 mg) were dissolved in 50 mL of distilled water to obtain 0.2 mM dye solutions, respectively. To test the adsorption preferences of **1** and **2** for different cationic dyes, 3 mg samples were dispersed in the above solutions (4 mL) to obtain **1**@dye and **2**@dye suspensions, whose absorbances were measured every hour. The maximum adsorption capacities of **1** and **2** for MG were measured by adding 3 mg samples to MG solutions of different volumes (4–8 mL), whose absorbances were measured every 2 h. In addition, anti-interference experiments of **1** and **2** for MG were performed by adding **1**/**2** (3 mg) to mixture solutions (4 mL) of MG and other dyes, and the absorbances of the above mixture solutions were recorded every hour.

The adsorption capacity (q_t , mg g⁻¹) at a desired time t and the removal efficiency (η , %) of **1** and **2** for dyes were obtained based on the following formulas:

$$q_t = \frac{C_0 - C_t}{m} V \quad (1)$$

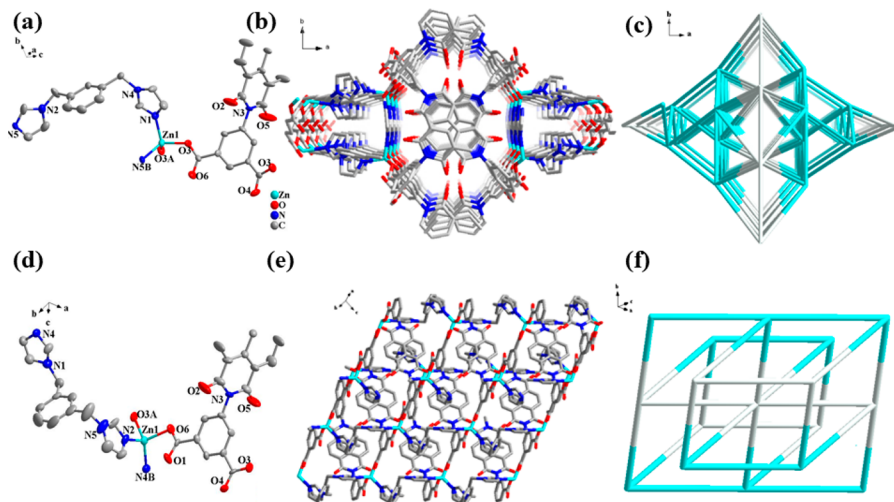


Figure 1. (a) The asymmetric unit of CP 1. Symmetrical code: A: $x, 1 - y, -0.5 + z$; B: $0.5 - x, -0.5 + y, 0.5 - z$; C: $1 - x, 2 - y, 2 - z$; D: $x, 1 - y, 0.5 + z$; E: $0.5 - x, 0.5 + y, 0.5 - z$; F: $1 - x, y - 1, 1.5 - z$; G: $1 - x, -1 + y, 3/2 - z$; H: $x, 1 - y, -1/2 + z$. (b) The 3D network of 1. (c) The topology of 1. (d) The asymmetric unit of CP 2. Symmetry code: A: $-1 + x, y, z$; B: $1 + x, y, 1 + z$; C: $1 - x, 1 - y, -z$; D: $1 + x, y, z$; E: $-1 + x, y, -1 + z$; F: $-x, 1 - y, -z$; G: $-x, 1 - y, -z$. (e) The 2D layered structure of 2. (f) The topology of 2.

$$\eta (\%) = \frac{C_0 - C_e}{C_0} \cdot 100\% \quad (2)$$

The equilibrium adsorption capacities of 1 and 2 for MG (q_e , mg g⁻¹) were calculated with eq 3:

$$q_e = \frac{C_0 - C_t}{m} V \quad (3)$$

where C_t (mg L⁻¹), C_0 , and C_e represent the concentration of suspension at sampling time t (h), the initial concentration, and the equilibrium concentration of the suspension, respectively.

2.6. Dye Desorption Tests. Samples of 3 mg of MG@1/MG@2 were added into 4 mL of distilled water, respectively. The above solutions were heated in a water bath at 65 °C. In addition, the color changes and absorbances of the MG@1 and MG@2 solutions were recorded every 12 h. After dye desorption tests, CPs 1 and 2 were taken out, washed three times with deionized water, and dried at room temperature for cyclic experiments.

3. RESULTS AND DISCUSSION

3.1. Structural Description. Structural analysis shows that 1 belongs to a monoclinic system with the $C2/c$ space group; its asymmetric unit consists of one Zn^{II} ion, half of the H₄BIPA-TC ligand; and one 1,3-bimb ligand. The Zn^{II} ion connects with two O atoms of the coordinated H₄BIPA-TC ligand and two N atoms from the 1,3-bimb ligand (Figure 1a). Furthermore, the Zn^{II} ion is linked by H₄BIPA-TC to obtain a two-dimensional (2D) layer structure (Figure S1a), and the adjacent 2D layers are bridged by the 1,3-bimb ligand to construct a porous three-dimensional (3D) framework (Figure 1b and Figure S1b). Topologically, as shown in Figure 1c, H₄BIPA-TC and Zn^{II} ions are regarded as a 4-c node, respectively, and the structure of 1 is simplified to a 2-node 4-c 3D network with the point symbol {6², 8⁴} {6⁴, 8²}₂.

2 belongs to monoclinic system and its space group is $P2_1/c$. The asymmetric unit is composed of one Zn^{II} ion, half of the H₄BIPA-TC linker and one 1,3-bimb ligand. Zn^{II} ion is four-coordinated and connected with two O atoms from the coordinated H₄BIPA-TC linker and two N atoms from 1,3-bimb ligand (Figure 1d). Zn^{II} ion is bridged with oxygen atoms of H₄BIPA-TC and N atoms of 1,3-bimb to form a 1D stepped chain and a spiral chain respectively (Figure S1c,d), which are

connected with Zn^{II} ions to form 2D layered network (Figure 1e). Topologically, the whole framework of 2 is simplified to a 2-node 4-c 2D framework with the point symbol {4, 6⁴, 8}₂ {4², 6⁴} (Figure 1f).

In addition, it can be seen from Figure S2a,b that 1 and 2 have different shapes; that is, 1 presents a petal-like morphology and 2 is rectangular block, which can be further confirmed by SEM morphologies of 1 and 2, as shown in Figure S2c,d. Meanwhile, EDS mapping images (Figures S3 and S4) confirmed the presence of C, N, O, and Zn elements in 1 and 2.

As shown in Figure S5, the N₂ adsorption–desorption behaviors of the sample were carried out at 77 K. The maximum adsorption capacities of 1 and 2 are 98.2 cm³ g⁻¹ (77 K, 1 bar) and 78.6 cm³ g⁻¹ (77 K, 1 bar), respectively. The BET specific surface areas of 1 and 2 are 266.2 and 135.4 m² g⁻¹, respectively. The adsorption isotherms of 1 and 2 belong to type I with pore sizes of 1.5 (1) and 1.3 nm (2), which was consistent with the structural information obtained from the crystal data. As displayed in Figure S6, the PXRD patterns of samples after gas adsorption are in good agreement with the PXRD patterns of the as-synthesized 1 and 2, indicating that 1 and 2 have good stability after gas adsorption–desorption tests.

3.2. Structural Stabilities of 1 and 2. The experimental PXRD patterns of 1 and 2 are almost identical with those simulated by single crystal data (Figure S7), indicating that the as-synthesized samples have good phase purity. The IR spectra of CPs 1 and 2 (Figure S8) showed that the peaks at 3449 and 3439 cm⁻¹ are attributed to the –O–H stretching vibration of water molecules, and the peak at 1580 cm⁻¹ is ascribed to the stretching vibration of –C=O– of H₄BIPA-TC. TG analyses of 1 and 2 were performed under a N₂ atmosphere (Figure S9). For 1, 8.43% of the weight loss before 240.9 °C was due to three-quarters of the DMF molecule (calcd 8.38%), and the structure of 1 began to collapse above 350 °C. As for CP 2, the weight loss mainly consists of three stages. At 90.1 °C, the weight loss of 3.34% was attributed to half of ethanol molecules (calcd 3.31%). Between 90.1 and 185.1 °C, the weight loss of 2.57% was attributed to the loss of a lattice water molecule (calcd 2.59%). Around 240 °C, the weight loss of 7.95% was ascribed to the loss

of a lattice DMF molecule (calcd 7.93%). Finally, the structure of **2** began to collapse above 388 °C.

3.3. Crystal Transformation. The synthetic conditions of **1** and **2** are the same except for reaction time, but **1** and **2** have completely different structures; that is, **1** shows 3D networks and **2** exhibits 2D layered structures. Compounds **1** and **2** are prepared under the same conditions except for the reaction time. The reaction rate to **1** is faster and the corresponding reaction is controlled by kinetics, while the reaction rate to **2** is slower and the corresponding reaction is controlled by thermodynamics. Interestingly, the transformation from single crystal **1** to **2** is only due to the prolongation of reaction time, which can be confirmed by structural analysis and PXRD patterns (Figure S10). By comparing their structures, it is clear that the dihedral angle between two H₄BIPA-TC ligands connected with Zn^{II} ion is 39.9° in **1** (Figure 2a), while two H₄BIPA-TC ligands are

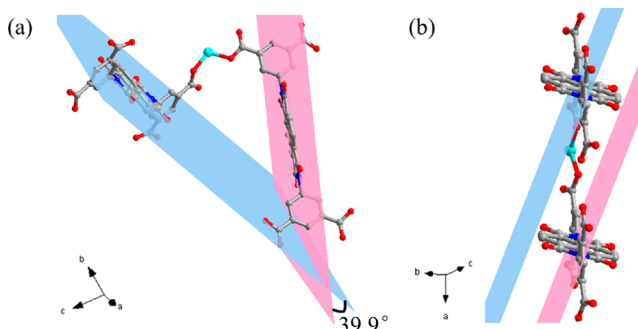


Figure 2. Dihedral angle between two H₄BIPA-TC ligands connected with Zn^{II} ion.

parallel in **2** (Figure 2b). Furthermore, the flexible 1,3-bimb exhibits a cis-configuration and adopts a bridging mode to coordinate with Zn ions, which is conducive to the formation of **1** with a 3D structure by further connecting with H₄BIPA-TC ligands. However, the flexible 1,3-bimb in **2** presents trans-configuration and adopts a terminal mode to coordinate with Zn ions, which prevents the structure of **2** from further extension, thus resulting in a 2D layered structure (Figure 3). In summary,

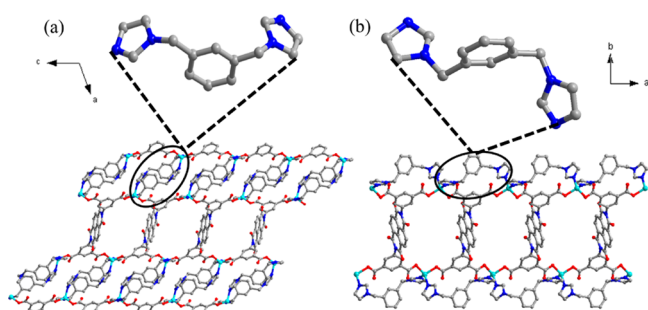


Figure 3. Configuration of 1,3-bimb in **1** (a) and **2** (b).

2 is a thermodynamic product, which is attributed to π–π interaction between benzene ring planes of H₄BIPA-TC ligands and the trans-conformation of the 1,3-bimb ligand; this is the reason for transformation from single crystal **1** to single crystal **2**.

3.4. Fluorescence Properties. As shown in Figure S11, the solid state fluorescence spectra of **1**, **2**, and H₄BIPA-TC were recorded at ambient temperature. The H₄BIPA-TC ligand exhibits a maximum emission peak at 465 nm ($\lambda_{\text{ex}} = 410$ nm). The emission peaks of **1** and **2** were observed at 530 and 535 nm,

respectively. The emission peaks of **1** and **2** were red-shifted compared with that of the free H₄BIPA-TC ligand, which is ascribed to the internal π*–π and π*–n transitions of the ligand.²⁹ The fluorescence intensity of **1** was higher than that of **2** due to the more compact topology of **1** (Figure 1c), which increases the rigid conformation and reduces nonradiative attenuation in the ligand.^{30,31} The fluorescence lifetimes and quantum yields (QYs) of **1** and **2** were 4.69 (**1**) and 4.55 ns (**2**) and 32.53 (**1**) and 30.25% (**2**), respectively (Figure S12).

Due to the excellent stability and fluorescence properties of **1** and **2**, the fluorescence sensing of **1** and **2** for different amino acids was explored. As displayed in Figure 4, compared with blank suspensions of **1** and **2**, the fluorescence intensities of **1** and **2** depend on different amino acids. It is worth noting that the fluorescence enhancement behavior of **1** and **2** was the most significant after detecting L-Glu suspension, indicating that **1** and **2** have the potential prospect to detect L-Glu in practical application.

To further investigate the sensitivity of **1** and **2** for detecting L-Glu, fluorescent gradient tests were also carried out after gradually adding 1 mM L-Glu. As exhibited in Figure 5a,b, the fluorescence intensities of **1** and **2** increased gradually with the increase of L-Glu concentration.

In addition, a linear behavior between the concentration of L-Glu and the fluorescence relative intensity (I_0/I) of **1** and **2** was observed by adding L-Glu in suspensions of **1** and **2** (Figure 5c,d), which can be described by $I_0/I = 7.76 \times 10^{-5}[\text{L-Glu}] + 1$ ($R^2 = 0.99$) and $I_0/I = 7.85 \times 10^{-4}[\text{L-Glu}] + 1$ ($R^2 = 0.99$) in the concentration ranges 0–10 and 0–60 μM, respectively. By the $3\sigma/K_{\text{sv}}$ formula (σ = standard error), the limits of detection (LODs) of **1** and **2** toward L-Glu were 0.10 and 0.13 μM, respectively,³² which were comparable to or much lower than those reported in the literature (Table S1).^{33,34}

To investigate the anti-interference performances of **1** and **2**, **1** and **2** (2 mg) were immersed in 2 mL aqueous solutions containing a mixture of L-Glu and other amino acids (1 mM) for 20 min and the fluorescence spectra of suspensions were recorded. As shown in Figure S13, the fluorescence enhancement still exists after the addition of other amino acid aqueous solutions, indicating that **1** and **2** have high sensing selectivity to L-Glu through the fluorescence enhancement effect. Therefore, **1** and **2** can be used as effective turn-on fluorescence sensors to detect L-Glu.

The cycling stabilities of **1** and **2** for the detection of L-Glu were investigated. As shown in Figure S14, the fluorescence intensities of **1** and **2** changed little compared with that of the as-synthesized sample after five cycles, which further confirmed the good stabilities of **1** and **2**.

3.5. Fluorescence Enhancement Mechanism. To reveal the fluorescence enhancement mechanism of L-Glu for **1** and **2**, a series of experiments, including PXRD, UV-vis spectra, and fluorescence lifetime, were carried out. First of all, the PXRD patterns of **1** and **2** after the detection of L-Glu were similar to those of the original samples (Figure S15), indicating that the structures of **1** and **2** were intact after L-Glu was detected. Therefore, the fluorescence enhancement of **1** and **2** was not caused by the collapse of their structures. Second, as shown in Figure S16, the absorbance of **1** and **2** after detecting L-Glu significantly enhanced, indicating that the fluorescence enhancement partially belongs to the absorbance caused enhancement (ACE);^{35,36} that is, the electrons of L-Glu@CP composite in the ground state can absorb more energy from the xenon lamp after the detection of L-Glu and then transmit to the excited state. In

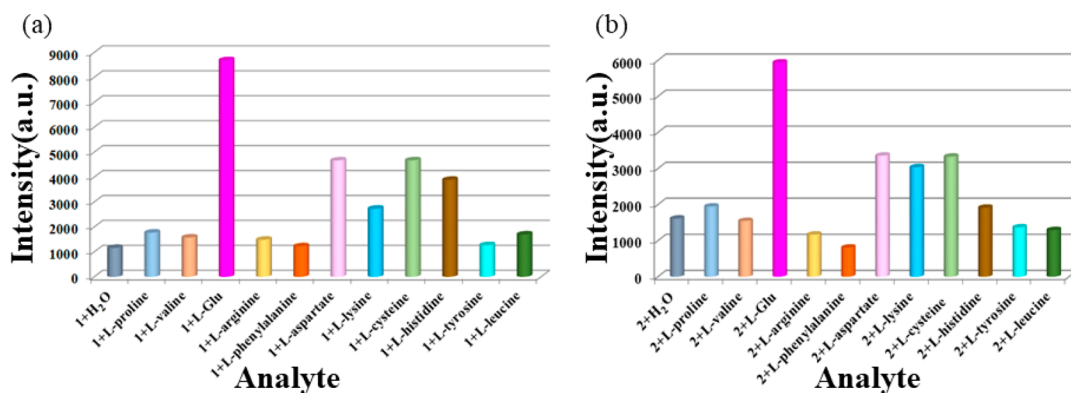


Figure 4. Fluorescence intensities of CPs **1** (a) and **2** (b) dispersed in aqueous solution containing various amino acids.

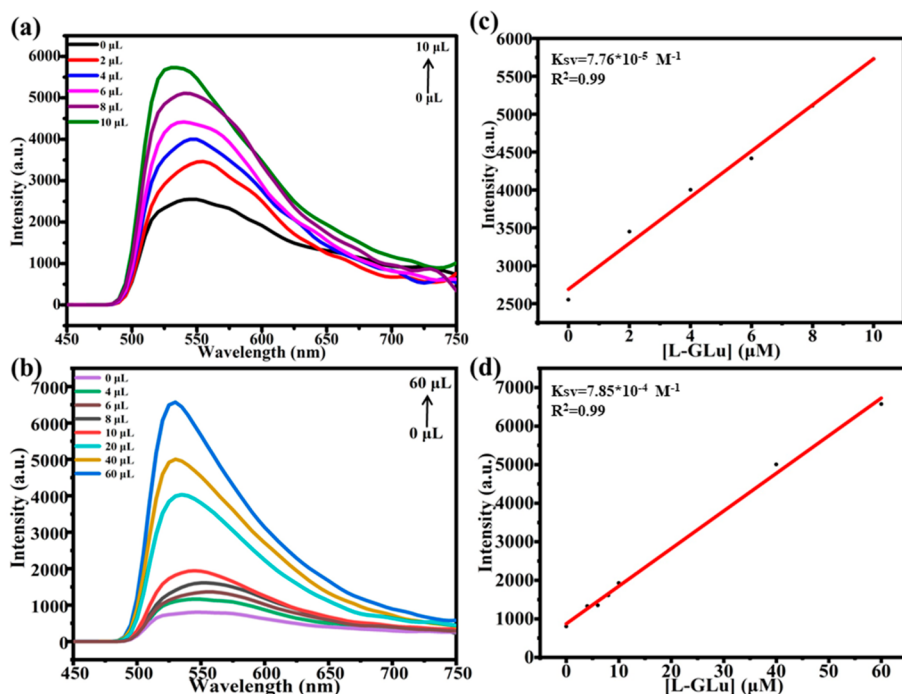


Figure 5. Emission spectra of **1** (a) and **2** (b) dispersed in different concentrations of L-Glu. Linear relationship between concentration of L-Glu and fluorescence intensity of **1** (c) and **2** (d).

addition, fluorescence titration spectra of L-Glu for **1** and **2** (Figure S17) showed that the position of the fluorescence peak did not change significantly, but the fluorescent spectrum increased with the rise of the L-Glu amount, indicating the presence of the ACE mechanism, which was also verified by the enhanced fluorescence lifetimes of **1** and **2** after the detection of L-Glu (Figure S12). In other words, the L-Glu@CP composite in the ground state can absorb more energy than the CPs themselves.

Finally, the energy levels of the highest occupied molecular orbital (HOMO) and the lowest unoccupied molecular orbital (LUMO) for L-Glu and H₄BIPA-TC were analyzed by using DFT at the B3LYP/6-31G* level to verify whether there is photoinduced electron transfer (PET).³⁷ As exhibited in Figure 6, the LUMO energy level of L-Glu exceeds that of H₄BIPA-TC, showing that the electrons can transfer from L-Glu to H₄BIPA-TC. In sum, the fluorescence enhancement mechanisms of **1** and **2** are attributed to ACE and PET.

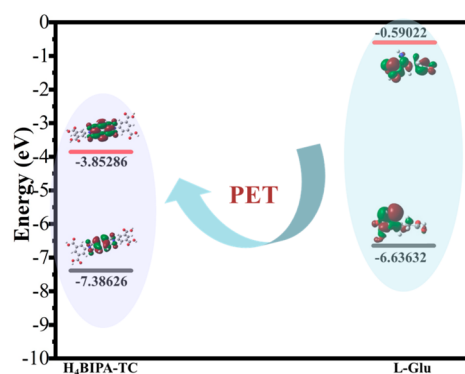


Figure 6. HOMO (black) and LUMO (red) values calculated of H₄BIPA-TC and L-Glu.

4. ADSORPTION STUDY

4.1. Adsorption. On the basis of structural characteristics of **1** and **2**, adsorption experiments of **1** and **2** for cationic dyes were

carried out. As exhibited in Figure 7 and Figures S18 and S19, compared with other dye suspensions, **1** and **2** have the most

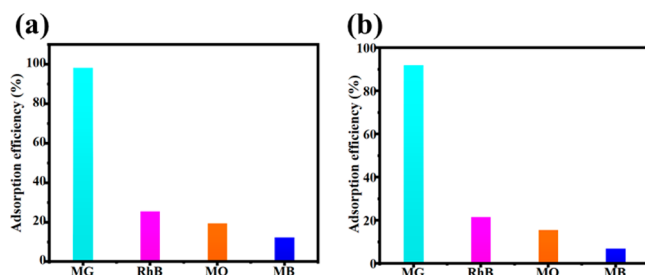


Figure 7. Adsorption efficiencies of **1** (a) and **2** (b) for MG, MO, RhB, and MB aqueous solutions.

significant adsorption capacities for MG, indicating that **1** and **2** have potential application prospects for removing MG in aqueous medium. Meanwhile, as shown in Figures S20 and S21, the adsorption of **1** and **2** for MG reached equilibrium after 48 h, and the absorbances of **1** and **2** were basically unchanged. The maximum adsorption capacities of **1** and **2** for MG were 351.06 (**1**) and 250.45 mg g⁻¹ (**2**), which were much higher than those reported (Table S2) in some literature.^{38–40} Besides, the adsorption kinetics of **1** and **2** for MG followed a quasi-second-order kinetic model based on kinetic data (Figure S22), and the correlation coefficients (R^2) were $R^2 = 0.9999$ (**1**) and $R^2 = 0.9998$ (**2**). It can be seen from Figure S23 that the adsorption process of **1** and **2** for MG followed the Freundlich isothermal model ($R^2 = 0.991$ for **1** and $R^2 = 0.989$ for **2**) and the value of the empirical constant (n) obtained by the Freundlich equation is less than 1, which indicates that the adsorption process of **1** and **2** for MG is monolayer surface adsorption.⁴¹

Furthermore, as displayed in Figures S24 and S25, the absorbance of **1@MG** decreased obviously when other competitive cationic dyes and MG coexisted, indicating that the adsorption process of **1** and **2** for MG was not affected by other dye molecules.

4.2. Desorption. The desorption experiments of **1** and **2** for MG showed that the color of the solution gradually changed from colorless to blue (Figure S26) and the absorbance of **1** and **2** increased from 0 to 1.5 (Figure 8), which verified that the MG molecules were successfully desorbed from the channel of **1** and **2**.

4.3. Recyclability of **1 and **2**.** The recyclability of adsorbent is very important for its practical application. As shown in Figure 9, after five adsorption–desorption cycles, the removal rates of **1**

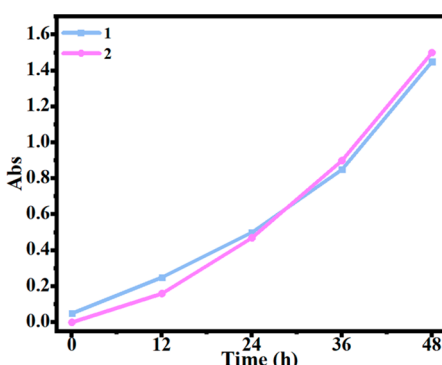


Figure 8. Absorbances of **1@MG** and **2@MG** at different times.

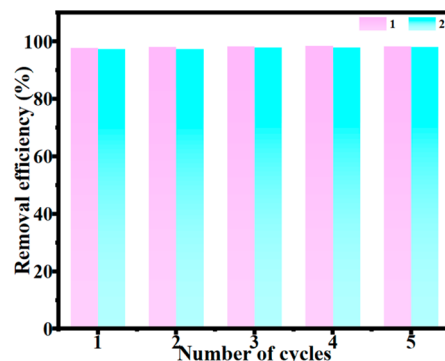


Figure 9. Recyclability of **1** and **2**.

and **2** for MG were still close to 100%, which showed that **1** and **2** have good recyclability. Meanwhile, the PXRD patterns of **1** and **2** after dye adsorption were in good agreement with the PXRD patterns of the original one (Figure S6), indicating that **1** and **2** have excellent structural stability after long-term adsorption of MG.

4.4. Adsorption Mechanism. Infrared (IR) experiments and theoretical calculations were carried out to reveal the adsorption mechanism of **1** and **2** for MG molecules.

First, the molecular size of MG (2.0 nm)⁴² is larger than the pore sizes of **1** (1.5 nm) and **2** (1.3 nm), which indicates the adsorption of **1** and **2** for MG occurs on the surface of their frameworks. Second, as illustrated in Figure S27, the benzene ring vibration peak intensity (1580 cm⁻¹) of **1** and **2** becomes weak after adsorption of MG molecules, which is attributed to the $\pi-\pi$ interaction between the conjugated benzene rings of **1** and **2** and the MG molecule.⁴³ The peak (1662 cm⁻¹) of the $-C=O$ groups in **1** and **2** became weak after adsorption of MG molecules, indicating that there was hydrogen bonding between **1/2** and MG molecules.⁴⁴ Furthermore, the calculation results show that the MG molecule exhibits electropositive and **1** and **2** are partially electronegative (Figure 10), which indicates that there is an electrostatic interaction between **1/2** and MG molecules. Meanwhile, as shown in Tables S4 and S5, the descending order of binding energy between **1/2** and dye molecules is 2117.36 kcal mol⁻¹ (MG@**1**) > 2021.93 kcal mol⁻¹ (RhB@**1**) > 888.52 kcal mol⁻¹ (MO@**1**) > 667.86 kcal mol⁻¹ (MB@**1**), 802.66 kcal mol⁻¹ (MG@**2**) > 789.36 kcal mol⁻¹ (RhB@**2**) > 766.02 kcal mol⁻¹ (MO@**2**) > 525.80 kcal mol⁻¹ (MB@**2**), respectively, which indicates that **1** and **2** have strong adsorption capacity for MG molecules.

To sum up, the adsorption mechanism of **1/2** for MG molecules can be attributed to $\pi-\pi$ interaction, hydrogen bonding, and electrostatic interaction between **1/2** and the MG molecule.

5. CONCLUSION

In a word, two time-induced novel Zn-CPs have been successfully constructed under the same conditions except for the hydrothermal reaction time. Meanwhile, the results showed single crystal **1** can be converted to single crystal **2** by the prolongation of reaction time, which can be confirmed by structure analysis and PXRD data. Fluorescence experiments showed that **1** and **2** displayed sensitive fluorescence turn-on detection for L-Glu with LODs of 0.10 (**1**) and 0.13 μ M (**2**). The fluorescence enhancement mechanisms of **1** and **2** were attributed to ACE and PET. In addition, dye adsorption experiments showed that **1** and **2** exhibited good adsorption

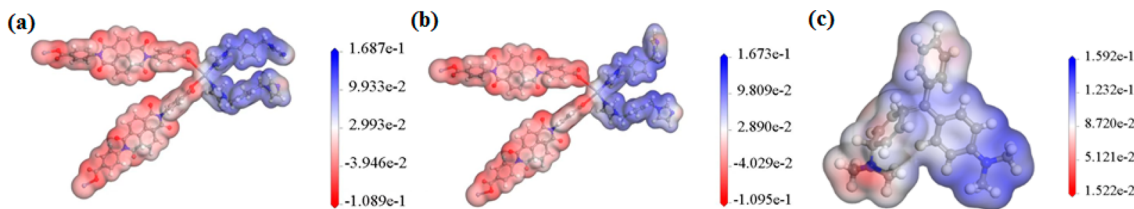


Figure 10. Surface electrostatic potential energies of **1** (a), **2** (b), and MG (c).

capacities for MG molecules and the maximum adsorption capacity reached 351.06 and 250.45 mg g⁻¹, respectively. The adsorption mechanism of **1/2** for MG molecules can be ascribed to $\pi-\pi$ interaction, hydrogen bonding, and electrostatic interaction between **1/2** and the MG molecule. Based on excellent fluorescence turn-on sensing properties and dye adsorption capacity, CPs **1** and **2**, as bifunctional materials with low cost and recyclability, have potential application prospects in the practical detection of L-Glu and the adsorption of MG dye.

■ ASSOCIATED CONTENT

§ Supporting Information

The Supporting Information is available free of charge at <https://pubs.acs.org/doi/10.1021/acs.cgd.2c01410>.

Detailed and additional results from crystallographic information, TGA, solid-state emission spectra, fluorescence fitting equations, cycle test experiments, PXRD patterns, UV-vis spectra, fluorescence lifetime curves ([PDF](#))

Accession Codes

CCDC [2104521](#) and [2104536](#) contain the supplementary crystallographic data for this paper. These data can be obtained free of charge via www.ccdc.cam.ac.uk/data_request/cif, or by emailing data_request@ccdc.cam.ac.uk, or by contacting The Cambridge Crystallographic Data Centre, 12 Union Road, Cambridge CB2 1EZ, UK; fax: +44 1223 336033.

■ AUTHOR INFORMATION

Corresponding Authors

Tuoping Hu – School of Chemical Engineering and Technology, North University of China, Taiyuan 030051, China;
[ORCID iD: 0000-0001-7437-3246](https://orcid.org/0000-0001-7437-3246); Email: hutuoping@nuc.edu.cn

Lingling Gao – Department of Chemistry, College of Science, Jinzhong University, Jinzhong 030619, China;
Email: 460381860@qq.com

Authors

Sai Ma – School of Chemical Engineering and Technology, North University of China, Taiyuan 030051, China

Yujuan Zhang – School of Chemical Engineering and Technology, North University of China, Taiyuan 030051, China; [ORCID iD: 0000-0002-2053-1410](https://orcid.org/0000-0002-2053-1410)

Complete contact information is available at:

<https://pubs.acs.org/10.1021/acs.cgd.2c01410>

Author Contributions

Sai Ma: Experiments, writing—original draft. Lingling Gao: Formal analysis. Jujuan Zhang: Supervision, writing—review. Tuoping Hu: Supervision, writing—review and editing, funding acquisition.

Notes

The authors declare no competing financial interest.

■ ACKNOWLEDGMENTS

The authors gratefully acknowledge the financial support of this work by the Shanxi Provincial Key Laboratory of Advanced Carbon Electrode Materials (202104010910019).

■ REFERENCES

- Wu, K.; Zheng, J.; Huang, Y.-L.; Luo, D.; Li, Y.-Y.; Lu, W.; Li, D. Cr₂O²⁻ inside Zr/Hf-based metal-organic frameworks: highly sensitive and selective detection and crystallographic evidence. *J. Mater. Chem. C* **2020**, *8*, 16974–16983.
- Cui, R.; Li, R.; Li, Z.; Wei, M.; Wang, X.; Li, X. A Tb-MOF anion, porous coordination framework constructed with oxalate ligand: Crystal structure, adsorption properties, and luminescence sensing. *Dyes Pigm.* **2021**, *195*, 109669.
- Altintas, C.; Altundal, O. F.; Keskin, S.; Yildirim, R. Machine Learning Meets with Metal Organic Frameworks for Gas Storage and Separation. *J. Chem. Infor. Modeling.* **2021**, *61*, 2131–2146.
- Li, W. Q.; Zhao, D. S.; Lei, N. N.; Wen, R. M.; Li, W. C.; Dou, M. Y.; Fan, L. M. Luminescence sensing and electrocatalytic redox performances of a new stable Cadmium(II) coordination polymer. *J. Solid. State. Chem.* **2023**, *317*, 123649.
- Li, Y.; An, J.-D.; Wang, T.-T.; Shi, Y.-F.; Huo, J.-Z.; Wu, X.-X.; Liu, Y.-Y.; Ding, B. An ultra-stable Cadmium(II) Coordination Framework Constructed From the new Bi-Functional Ligand and Application as Fluorescent Probe for Acetylacetone and Antibiotics. *Dyes. Pigm.* **2021**, *186*, 109039.
- Xu, Z.; Han, L.-L.; Zhuang, G.-L.; Bai, J.; Sun, D. In Situ Construction of Three Anion-Dependent Cu(I) Coordination Networks as Promising Heterogeneous Catalysts for Azide-Alkyne "Click" Reactions. *Inorg. Chem.* **2015**, *54*, 4737–4743.
- Wang, J.; Zhou, L.; Rao, C.; Wang, G.-L.; Jiang, F.; Singh, A.; Kumar, A.; Liu, J. Two 3D supramolecular isomeric Zn(II)-MOFs as photocatalysts for photodegradation of methyl violet dye. *Dyes. Pigm.* **2021**, *190*, 109285.
- Chen, H. T.; Fan, L. M.; Lv, H. X.; Zhang, X. T. Robust Anionic Ln^{III}-Organic Frameworks: Chemical Fixation of CO₂, Tunable Light Emission, and Fluorescence Recognition of Fe³⁺. *Inorg. Chem.* **2020**, *59*, 13407–13415.
- Lv, H. X.; Chen, H. T.; Fan, L. M.; Zhang, X. T. Nanocage-Based Tb³⁺-Organic Framework for Efficiently Catalyzing the Cycloaddition Reaction of CO₂ with Epoxides and Knoevenagel Condensation. *Inorg. Chem.* **2022**, *61*, 15558–15568.
- Yao, S.-L.; Liu, S.-J.; Tian, X.-M.; Zheng, T.-F.; Cao, C.; Niu, C.-Y.; Chen, Y.-Q.; Chen, J.-L.; Huang, H.; Wen, H.-R. A Zn^{II}-Based Metal-Organic Framework with a Rare tcj Topology as a Turn-On Fluorescent Sensor for Acetylacetone. *Inorg. Chem.* **2019**, *58*, 3578–3581.
- Yan, Z.-H.; Li, X.-Y.; Liu, L.-W.; Yu, S.-Q.; Wang, X.-P.; Sun, D. Single-Crystal to Single-Crystal Phase Transition and Segmented Thermochromic Luminescence in a Dynamic 3D Interpenetrated Ag-I Coordination Network. *Inorg. Chem.* **2016**, *55*, 1096–1101.
- Wang, Z.; Li, X.-Y.; Liu, L.-W.; Yu, S.-Q.; Feng, Z.-Y.; Tung, C.-H.; Sun, D. Beyond Clusters: Supramolecular Networks Self-

- Assembled from Nanosized Silver Clusters and Inorganic Anions. *Chem.—Eur. J.* **2016**, *22*, 6830–6836.
- (13) Chen, H. T.; Zhang, T.; Liu, S. R.; Lv, H. X.; Fan, L. M.; Zhang, X. T. Fluorine-Functionalized NbO-Type {Cu₂}-Organic Framework: Enhanced Catalytic Performance on the Cycloaddition Reaction of CO₂ with Epoxides and Deacetalization-Knoevenagel Condensation. *Inorg. Chem.* **2022**, *61*, 11949–11958.
- (14) Liu, S. R.; Chen, H. T.; Lv, H. X.; Qin, P. L.; Fan, L. M.; Zhang, X. T. Chemorobust 4p-5p {InPb}-organic framework for efficiently catalyzing cycloaddition of CO₂ with epoxides and deacetalization-Knoevenagel condensation. *Mater. Today Chem.* **2022**, *24*, 100984.
- (15) Chen, D.-M.; Ma, X.-Z.; Shi, W.; Cheng, P. Solvent-Induced Topological Diversity of Two Zn(II) Metal-Organic Frameworks and High Sensitivity in Recyclable Detection of Nitrobenzene. *Cryst. Growth Des.* **2015**, *15*, 3999–4004.
- (16) Zhou, H.-F.; He, T.; Yue, K.-F.; Liu, Y.-L.; Zhou, C.-S.; Yan, N.; Wang, Y.-Y. Temperature-Induced Syntheses, Iodine Elimination, Enantiomers Resolution, and Single-Crystal-to-Single-Crystal Transformation of Imidazole-Co(II) Coordination Polymers with Amino-isophthalic Acid as Co-Ligand. *Cryst. Growth Des.* **2016**, *16*, 3961–3968.
- (17) Wang, W.; He, Y.; Gao, Y.; Gao, H.; Deng, L.; Gui, Q.; Cao, Z.; Yin, Y.; Feng, Z. A peptide aptamer based electrochemical amperometric sensor for sensitive L-glutamate detection. *Bioelectrochemistry* **2022**, *146*, 108165.
- (18) Li, G.; Wang, T.; Zhou, S.; Wang, J.; Lv, H.; Han, M.; et al. New highly luminescent 3D Tb(III)-MOF as selective sensor for antibiotics. *Inorg. Chem. Commun.* **2021**, *130*, 108756.
- (19) Jiao, Z.-H.; Jiang, X.-L.; Hou, S.-L.; Tang, M.-H.; Zhao, B. Highly Sensitive and Selective Luminescence Sensor Based on Two-Fold Interpenetrated MOFs for Detecting Glutamate in Serum. *Inorg. Chem.* **2020**, *59*, 2171–2177.
- (20) Zhu, J. Y.; Xia, T. F.; Cui, Y. J.; Yang, Y.; Qian, G. D. A turn-on MOF-based luminescent sensor for highly selective detection of glutathione. *J. Solid. State. Chem.* **2019**, *270*, 317–323.
- (21) Zhang, Y. J.; Gao, L. L.; Ma, S.; Hu, T. P. A multifunctional metal-organic framework with a μ₃-OH⁻ site for gas and vapor sorption and selective detection of nitrofurantoin. *J. Mater. Chem. C* **2022**, *10*, 1136–1143.
- (22) Gao, M.; Wang, Z.; Yang, C.; Ning, J.; Zhou, Z.; Li, G. Novel magnetic graphene oxide decorated with persimmon tannins for efficient adsorption of malachite green from aqueous solutions. *Colloid. Surf. A* **2019**, *566*, 48–57.
- (23) Miri-Jahromi, A.; Mohammady Maklavy, D.; Rouzitalab, Z.; Ghaemi Khiavi, S.; Ghasemiy, E.; Khedri, M.; Rezvantalab, S.; Sharafinia, S.; Rashidi, A.; Maleki, R. Engineering of two-dimensional monolayers to phenolic compounds removal from wastewater: An experimental and computational insight. *J. Mol. Liq.* **2022**, *362*, 119784.
- (24) de Araujo, C. M. B.; Ghislandi, M. G.; Rios, A. G.; da Costa, G. R. B.; do Nascimento, B. F.; Ferreira, A. F. P.; da Motta Sobrinho, M. A.; Rodrigues, A. E. Wastewater treatment using recyclable agar-graphene oxide biocomposite hydrogel in batch and fixed-bed adsorption column: Bench experiments and modeling for the selective removal of organics. *Colloid. Surf. A* **2022**, *639*, 128357.
- (25) Boudechiche, N.; Fares, M.; Ouyahia, S.; Yazid, H.; Trari, M.; Sadaoui, Z. Comparative study on removal of two basic dyes in aqueous medium by adsorption using activated carbon from *Ziziphus lotus* stones. *Microchem. J.* **2019**, *146*, 1010–1018.
- (26) Golmohammadi, F.; Hazrati, M.; Safari, M. Removal of reactive yellow 15 from water sample using a magnetite nanoparticles coated with covalently immobilized dimethyl octadecyl (3-(trimethoxysilylpropyl))ammonium chloride ionic liquid. *Microchem. J.* **2019**, *144*, 64–72.
- (27) Liu, L.-L.; Chen, J.; Zhang, Y.; Yu, C.-X.; Du, W.; Sun, X.-Q.; et al. Fabrication of ultrathin single-layer 2D metal-organic framework nanosheets with excellent adsorption performance via a facile exfoliation approach. *J. Mater. Chem. A* **2021**, *9*, 546–555.
- (28) Zhang, Y. J.; Gao, L. L.; Ma, S.; Hu, T. P. Cd (II) coordination polymer as a strip based fluorescence sensor for sensing Fe³⁺ ions in aqueous system. *Spectrochim. Acta A Mol. Biomol. Spectrosc.* **2022**, *267*, 120525.
- (29) Cui, P.; Chen, Z.; Gao, D.; Zhao, B.; Shi, W.; Cheng, P. Syntheses, Structures, and Photoluminescence of a Series of Three-Dimensional Cd(II) Frameworks with a Flexible Ligand, 1,5-Bis(5-tetrazolo)-3-oxapentane. *Cryst. Growth Des.* **2010**, *10*, 4370–4378.
- (30) Allendorf, M. D.; Bauer, C. A.; Bhakta, R. K.; Houk, R. J. T. Luminescent metal-organic frameworks. *Chem. Soc. Rev.* **2009**, *38*, 1330–1352.
- (31) Dutta, B.; Jana, R.; Bhanja, A. K.; Ray, P. P.; Sinha, C.; Mir, M. H. Supramolecular Aggregate of Cadmium(II)-Based One-Dimensional Coordination Polymer for Device Fabrication and Sensor Application. *Inorg. Chem.* **2019**, *58*, 2686–2694.
- (32) Han, L.-J.; Kong, Y.-J.; Hou, G.-Z.; Chen, H.-C.; Zhang, X.-M.; Zheng, H.-G. A Europium-based MOF Fluorescent Probe for Efficiently Detecting Malachite Green and Uric Acid. *Inorg. Chem.* **2020**, *59*, 7181–7187.
- (33) Zhao, Y. F.; Wan, M.-Y.; Bai, J.-P.; Zeng, H.; Lu, W. G.; Li, D. pH-Modulated luminescence switching in a Eu-MOF: rapid detection of acidic amino acids. *J. Mater. Chem. B* **2019**, *7*, 11127–11133.
- (34) Zhao, X.; Zhang, Y.; Han, J.; Jing, H.; Gao, Z.; Huang, H.; Wang, Y.; Zhong, C. Design of “turn-on” fluorescence sensor for L-Cysteine based on the instability of metal-organic frameworks. *Microporous Mesoporous Mater.* **2018**, *268*, 88–92.
- (35) Wang, M.; Guo, L.; Cao, P. D. Metal-organic framework as luminescence turn-on sensor for selective detection of metal ions: Absorbance caused enhancement mechanism. *Sens. Actuators. B* **2018**, *256*, 839–845.
- (36) Chen, W.-M.; Meng, X.-L.; Zhuang, G.-L.; Wang, Z.; Kurmoo, M.; Zhao, Q.-Q.; Wang, X.-P.; Shan, B.; Tung, C.-H.; Sun, D. A superior fluorescent sensor for Al³⁺ and UO₂²⁺ based on a Co(II) metal-organic framework with exposed pyrimidyl Lewis base sites. *J. Mater. Chem. A* **2017**, *5*, 13079–13085.
- (37) Zhu, K.; Wu, J. K.; Fan, R. Q.; Cao, Y.; Lu, H. Y.; Wang, B. W.; Zheng, X. B.; et al. Selective adsorption and detection of p-arsanilic acid on MOF-on-MOF heterostructure induced by nitrogen-rich self-assembly template. *Chem. Eng. J.* **2022**, *427*, 131483.
- (38) Mohammadi, A.; Daemi, H.; Barikani, M. Fast removal of malachite green dye using novel superparamagnetic sodium alginate-coated Fe₃O₄ nanoparticles. *Int. J. Biol. Macromol.* **2014**, *69*, 447–455.
- (39) Huo, S.-H.; Yan, X.-P. Metal-organic framework MIL-100(Fe) for the adsorption of malachite green from aqueous solution. *J. Mater. Chem.* **2012**, *22*, 7449–7455.
- (40) Mahmoud, R. K.; Taha, M.; Zaher, A.; Amin, R. M. Understanding the physicochemical properties of Zn-Fe LDH nanostructure as sorbent material for removing of anionic and cationic dyes mixture. *Sci. Rep.* **2021**, *11*, 21365.
- (41) Wang, W.; Wang, Z. J.; Li, K.; Liu, Y. X.; Xie, D. L.; Shan, S. Y.; He, L.; Mei, Y. Enhanced adsorption of aqueous chlorinated aromatic compounds by nitrogen auto-doped biochar produced through pyrolysis of rubber-seed shell. *Environ. Technol.* **2021**, DOI: 10.1080/09593330.2021.1980829.
- (42) Shi, Z.; Li, L.; Xiao, Y.; Wang, Y.; Sun, K.; Wang, H.; et al. Synthesis of mixed-ligand Cu-MOFs and their adsorption of malachite green. *RSC. Adv.* **2017**, *7*, 30904–30910.
- (43) Zhao, L.; Lv, W.; Hou, J. Y.; Li, Y. J.; Duan, J. L.; Ai, S. Y. Synthesis of magnetically recyclable g-C₃N₄/Fe₃O₄/ZIF-8 nanocomposites for excellent adsorption of malachite green. *Microchem. J.* **2020**, *152*, 104425.
- (44) Zheng, W. H.; Xu, Z. S.; Zhang, X. Highly efficient adsorption behavior of mesoporous Co-HDIPT toward both anionic and cationic organic dyes. *J. Porous Mater.* **2022**, *29*, 795–806.